Determination of linear viscoelastic properties of an entangled polymer melt by probe rheology simulations

Mir Karim, Tsutomu Indei, Jay D. Schieber, and Rajesh Khare

Phys. Rev. E **93**, 012501 — Published 25 January 2016

DOI: 10.1103/PhysRevE.93.012501

Determination of Linear Viscoelastic Properties of an Entangled Polymer Melt by Probe Rheology Simulations

Mir Karim,[1] Tsutomu Indei,[2] Jay D. Schieber,[2,3,4] and Rajesh Khare[1,*]

[1]*Department of Chemical Engineering,*
Texas Tech University, Box 43121, Lubbock, TX 79409, USA
[2]*Center for Molecular Study of Condensed Soft Matter,*
and Department of Chemical and Biological Engineering,
Illinois Institute of Technology, 3440 S. Dearborn Street, Chicago, Illinois 60616, USA
[3]*Department of Physics, Illinois Institute of Technology,*
3101 South Dearborn Street, Chicago, IL 60616, USA
[4]*Department of Applied Mathematics, Illinois Institute of Technology,*
10 West 32nd Street, Chicago, IL 60616, USA[†]

Abstract

Particle rheology is used to extract the linear viscoelastic properties of an entangled polymer melt from molecular dynamics simulations. The motion of a stiff, approximately spherical particle is tracked in both passive and active modes. We demonstrate that the dynamic modulus of the melt can be extracted under certain limitations using this technique. As shown before for unentangled chains [Karim et al., Phys. Rev. E **86**, 051501 (2012)], the frequency range of applicability is substantially expanded when both particle and medium inertia are properly accounted for by using our inertial version of the generalized Stokes-Einstein relation (IGSER). The system used here introduces an entanglement length d_T, in addition to those length scales already relevant: monomer bead size d, probe size R, polymer radius of gyration R_g, simulation box size L, shear wave penetration length Δ, and wave period Λ. Previously, we demonstrated a number of restrictions necessary to obtain the relevant fluid properties: continuum approximation breaks down when $d \gtrsim \Lambda$; medium inertia is important and IGSER is required when $R \gtrsim \Lambda$; and the probe should not experience hydrodynamic interaction with its periodic images, $L \gtrsim \Delta$. These restrictions are also observed here. A simple scaling argument for entangled polymers shows that the simulation box size must scale with polymer molecular weight as M_w^3. Continuum analysis requires the existence of an added mass to the probe particle from the entrained medium, but was not observed in the earlier work for unentangled chains. We confirm here that this added mass is necessary only when the thickness L_S of the shell around the particle that contains the added mass, $L_S > d$. We also demonstrate that the IGSER can be used to predict particle displacement over a given time scale from knowledge of medium viscoelasticity; such ability will be of interest for designing nanoparticle-based drug delivery.

* Email: rajesh.khare@ttu.edu

† Email: schieber@iit.edu

I. INTRODUCTION

Microrheology has evolved as a reliable experimental technique to extract the linear viscoelastic properties of complex fluids using either active or passive modes, and either single-point or two-point statistics [1–3]. Single-point rheology tracks the motion of a single spherical particle, whereas two-point rheology follows the hydrodynamic interaction of two such particles. Passive techniques rely on thermal motion of particles to probe the system, whereas active modes apply external oscillatory forces to move the particles. These techniques have become sufficiently reliable that even commercial passive, single-point microrheometers are available. The particles can be tracked by diffusing wave spectroscopy [4], laser interferometry [5], optical laser tweezers [6], or video tracking in either passive or active modes [2].

Since the required sample size is order one microliter, microrheology is well suited for expensive or scarce materials. However, materials of high modulus ($\gtrsim$ 10kPa) are problematic for passive microrheology, since probe motion is then hard to detect. This restriction is not a concern for many important materials, which are sufficiently soft; one thus finds examples of microrheology on colloidal suspensions [7–9], polymer gels [5], cells [10, 11], associated and flexible polymer solutions [12, 13], micellar solutions [14] and biological polymer networks like F-actin [15–17].

Rigorous data analysis for singe-point passive microrheology utilizes the generalized Stokes-Einstein relation (GSER), or at sufficiently high frequencies, the inertial GSER (IGSER) [18]. This relation assumes that (1) the probe particle sees the medium as a continuum, (2) that deformations of the medium due to the particle displacement are sufficiently small that the medium can be treated in the linear viscoelastic regime, (3) the fluctuation-dissipation theorem applies, and (4) the probe particle experiences no hydrodynamic interaction with nearby surfaces. The first assumption requires that the material microstructure be smaller than the probe diameter. However, the material may have heterogeneity (say polymer concentration fluctuations) on length scales larger than the probe diameter, in which case the technique can be used to measure local properties in systems such as intracellular compartments [19] and glassy materials [20]. This knowledge of local linear viscoelasticity obtained from probe microrheology can be useful for predicting local transport phenomena in practical applications such as the motion of drug carrying nanopar-

ticles in mucus [21] and the motion of filler particles in polymer composite materials [22]. By definition, passive microrheology remains in the linear regime guaranteeing that assumption (2) is valid. If active microrheology is used, the amplitude of the probe displacements needs to remain much smaller than the probe size. As regards to the third assumption, the fluctuation-dissipation theorem is otherwise very broadly applicable, but is not obeyed for systems with molecular motors (so-called "active gels"), which convert chemical energy into kinetic energy or force. The fourth assumption may be violated if there is a nearby solid surface, or in simulations, if the periodic boundary conditions place image particles too close to the probe. Two-point rheology analysis makes similar assumptions, but relies on hydrodynamic interaction between two probes. This interaction cannot be handled exactly, and various mathematical approximations can be employed with a high degree of accuracy [23–25].

If the intention is to use probe rheology for capturing the bulk linear viscoelastic behavior, then caution has to be exercised in the interpretation of the local linear viscoelasticity determined in this case. The most important issue is the interplay of physics occurring on different length scales. The length scales of interest for this purpose are: probe particle size, material microstructural length i.e. polymer network mesh length and the chain size [15, 26]. For traditional microrheological analysis to be valid [27, 28], the probe size should be large enough so that it can feel the surrounding medium as a continuum; this allows application of the GSER [2]. In the other limit, if the probe is of comparable or smaller size than the polymer segment, it will not sample the continuum properties of the medium [29].

On the theoretical side, an approach for determining the viscoelastic properties of a medium by analyzing the velocity autocorrelation function of a suspended particle has been proposed [30, 31]. On the other hand, some of us recently addressed several issues involving particle and medium inertia in single- and two-particle microrheology [24, 25, 32, 33]. For single-particle microrheology, a safe way of eliminating particle inertia was argued and proper Brownian dynamics simulations for inertia-less particles were demonstrated for some synthetic viscoelastic fluids [34]. For two-particle microrheology, effects of multiple wave reflections between the trapped particles [24], compressibility of the medium [25], and finite wave travel time [24, 25] were studied.

In our previous work [18], we studied probe rheology in a model unentangled polymer melt by analyzing the molecular dynamics (MD) simulation data using continuum mechanics.

We showed that the effects of particle and medium inertia need to be explicitly accounted for in such analysis to reach agreement with linear viscoelasticity determined by Green-Kubo or small-amplitude oscillatory flow. The key equation is the inertial Generalized Stokes Einstein relation (IGSER), obtained by the solution of unsteady transient motion of a spherical particle in a linear viscoelastic fluid [35, 36]; IGSER is used to extract the viscoelastic moduli of the medium from the probe particle motion.

Kuhnhold and Paul [37, 38] also simulated both active and passive microrheology in a melt of unentangled bead-spring chains. However, they observed disagreement between the two approaches, and suggested that the inertial generalized Stokes relation (and by inference, the GSR) is incorrect, since it does not incorporate rheological memory effects. However, the generalized Stokes relation is not an assumption, but rather the result of a mathematical theorem utilizing the correspondence principle [35, 36]. It exploits the convolution theorem in taking the Fourier transform of the memory integral that exists in linear viscoelastic theory. As a result, the generalized Stokes relation has a form identical to that arising from the Newtonian constitutive equation in the frequency domain, and includes all necessary memory effects. Its strongest, maybe only, assumption is that the probe bead experiences a continuum with a well-defined dynamic modulus—an assumption implicit in their work. There is another, more likely, reason for their observed discrepancy. First, their simulation box had edge length only one sixth of our simulation, so would contain artifactual hydrodynamic interaction between periodic images of the probe particle over a much greater frequency range. For the active rheology, they reported estimates of the dynamic modulus at very high frequencies at which these artifactual hydrodynamic interactions may not be significant, but at the same time, these frequencies ($\omega \geq 1$) are comparable or above the characteristic Lennard-Jones time scale [38]. In our previous simulations of an unentangled system [18], we observed a crossover from the Basset-force dominated motion to the ballistic motion of the probe on a very similar time range as that studied by Kuhnhold and Paul. There we showed that the relaxation modulus could hence not be reliably extracted from the probe motion signal for frequencies above 0.3, depending on available statistics. Since Kuhnhold and Paul report dynamic modulus values above $\omega = 1$ only, one should expect very large uncertainty in the estimates. More puzzling is their observation that over this frequency range, omitting inertia from the analysis yields positive storage moduli, while many of the mathematical variants of the expression containing inertia used by them exhibit negative

values of the moduli; our previous simulations showed behavior exactly opposite to theirs at high frequencies—that use of GSER yielded unphysical values of the moduli whereas IGSER yielded values that were in quantitative agreement with NEMD and Green-Kubo results.

In this work, we extend the IGSER approach to study probe rheology in an entangled polymer melt in both passive and active modes. This system exhibits richer physics than the unentangled system because of an additional relevant length scale: the entanglement spacing d_T. We examine the interaction of this new length scale with those already seen in the unentangled system: monomer bead size (d), probe size (R), chain size (R_g), wave length (Λ) and penetration depth (Δ) of the shear wave, and the simulation system size (L). We demonstrate that the linear viscoelasticity of the entangled polymer melt can be quantified using particle rheology simulations, and we identify the frequency range over which the analysis is valid. In a further important extension, we also demonstrate that if the medium viscoelastic spectrum is available, then IGSER can be used to predict nanoparticle displacement in the medium over a wide range of time scales.

II. COMPUTATIONAL METHOD

A. Simulation details

The system studied in this work consists of a nanoparticle (NP) that is embedded in a weakly entangled (number of beads N = 80) polymer melt. There are two types of beads in our system: polymer and nanoparticle beads. All beads interact with each other by either the regular Lennard-Jones (LJ) potential or the purely repulsive LJ potential (WCA type). Specifically monomer beads from the same chain or from different chains interact with each other by the WCA potential [39],

$$U_{WCA}(r) = \begin{cases} 4\varepsilon_{pp}\left(\left(\frac{\sigma_{pp}}{r}\right)^{12} - \left(\frac{\sigma_{pp}}{r}\right)^{6} + \frac{1}{4}\right), & r \le r_{c,pp} = 2^{1/6}\sigma_{pp} \\ 0, & r > r_{c,pp} \end{cases}$$

where r is the monomer-monomer pairwise distance and ε_{pp}, σ_{pp}, $r_{c,pp}$ are the LJ energy, diameter and cut-off distance parameters respectively. The suffix pp in the expression represents pairwise monomer-monomer bead (from polymer chains) interaction. All quantities reported in this work are nondimensionalized using σ_{pp}, ε_{pp} and m_p (polymer bead mass).

Here we note that, in reduced units, monomer bead size is $d = \sigma_{pp} = 1$. For nanoparticle-nanoparticle bead interactions, we use the same interaction potential with $\sigma_{nn} = 1$ and $\varepsilon_{nn} = 1$ and the same cut-off distance $r_{c,nn} = r_{c,pp}$. Since our continuum analysis assumes that the no-slip boundary condition holds at the nanoparticle-polymer interface, the full LJ potential along with $\sigma_{np} = 1$, $\varepsilon_{np} = 2$ and $r_{c,np} = 2.3$ was used to eliminate slip between the nanoparticle and the medium [40, 41]. Chain connectivity was modeled by using FENE (Finitely Extensible Nonlinearly Elastic) springs with potential [42], $U_{\text{FENE}} = -\frac{1}{2}KQ^2 \ln\left[1 - \left(\frac{r}{Q}\right)^2\right]$; the values of the parameters being $K = 30$ and $Q = 3/2$. The spherical nanoparticle with a rough surface was obtained by carving out a sphere of radius, $R_{\text{nominal}} = R = 12$ [41], from a FCC crystal lattice structure with lattice spacing value of 1.42. To maintain the rigidity of the nanoparticle, we connected each nanoparticle bead with its nearest neighbors by harmonic bonds, $U_{\text{Harmonic}} = \frac{1}{2}k_{\text{bond}}\left(b - b_0\right)^2$, where force constant $k_{\text{bond}} = 500$, and b_0 is the equilibrium bond distance as determined by the original crystal structure. The ability of this potential to maintain the rigid structure of the nanoparticle was established in previous work [41]. All simulations were carried out at temperature, $T = 1$ and density, $\rho = 0.85$, using a time step $\Delta t = 0.003$ for passive rheology simulations, and a range of time step values from Δt =0.001795—0.0027 for the active rheology simulations (different values were used for different frequencies). For all of our calculations, we used a cubic simulation box of edge length $L = 150$. The probe rheology results were compared with values of the complex shear modulus $G^*(\omega)$, obtained from the non-equilibrium molecular dynamics (NEMD) simulation [43]. For this purpose, small amplitude oscillatory shear NEMD simulations were performed at the same state point. In this technique, oscillatory shear is applied to the model system by a combination of modification of the equation of motion and application of the sliding-brick periodic boundary conditions and the moduli are determined by monitoring the resulting stress developed in the system as a function of time.[44] All of the simulations were performed at constant NVT (number of beads, volume and temperature) conditions with a Nosé-Hoover thermostat [45] using the LAMMPS [46] simulation package.

B. Continuum Mechanics Analysis:

The viscoelastic properties of the medium are obtained by analyzing the particle motion using continuum mechanics. The analysis procedure is described in detail in our previous work [18]. For the sake of completeness, a short summary is presented here. We write a generalized Langevin equation for the probe particle motion in a complex medium

$$m_{\text{bare}}\frac{d^2\mathbf{r}_b(t)}{dt^2} = -\int_{-\infty}^{t}\zeta(t-t')\frac{d\mathbf{r}_b(t')}{dt'}dt' + \mathbf{f}_{ex}(t) + \mathbf{f}_{\text{B}}(t), \tag{1}$$

where m_{bare} and $\mathbf{r}_b(t)$ are the probe particle mass (bare mass) and displacement, $\zeta(t-t')$ is the frictional memory tensor, while $\mathbf{f}_{ex}(t)$ and $\mathbf{f}_{\text{B}}(t)$ are the external conservative and Brownian forces acting on the particle, respectively. Using the fluctuation-dissipation theorem along with the generalized Stokes relation, and accounting for medium and particle inertia [32, 33], the generalized Langevin equation in the frequency domain takes the form [18]

$$\frac{6\pi RG^*(\omega)}{i\omega} + 6\pi R^2\sqrt{\rho G^*(\omega)} + i\omega m_{\text{eff}} = Z^*(\omega) \tag{2}$$

where ρ is the density of the medium. The first term on the left side of Eq.2 is the Stokes drag, the second term is the Basset force which has its origin in the medium inertia, and the third term is the effective inertial force contribution from the probe particle. In the third term, the effective mass of the moving particle in the medium is defined according to continuum mechanics as: $m_{\text{eff}} = m_{\text{bare}} + m_{\text{add}}$ [47]. The effective particle mass thus comprises of the bare mass of the particle m_{bare} and the added mass from the medium $m_{\text{add}} = \frac{2}{3}\pi R^3\rho$, that results from the medium inertia.

The expression obtained by solving Eq. (2) for the dynamic modulus is

$$\begin{aligned} G^*(\omega) = {} & \frac{i\omega Z^*(\omega)}{6\pi R} + \frac{m_{\text{eff}}\omega^2}{6\pi R} \\ & + \frac{R^2\omega^2}{2}\left[\sqrt{\rho^2 + \frac{2\rho}{3\pi R^3}\left(\frac{Z^*(\omega)}{i\omega} - m_{\text{eff}}\right)} - \rho\right]. \end{aligned} \tag{3}$$

We have verified that for both active and passive rheology, use of "bare" or "hydrodynamic" radii values (12 and 12.31, respectively) yield effectively the same results. We note here that for these calculations, the hydrodynamic radius of the probe particle is taken as the radius of the spherical region around the probe from which the centers of the medium particles are excluded [40]. The friction function $Z^*(\omega)$ assumes different forms in the active and the passive rheology approaches. Separate considerations for these active and passive modes are described in what follows.

1. Active rheology:

In the active mode, the particle motion is realized by subjecting it to an external sinusoidal oscillatory force, $\Re e\left\{\mathbf{F}_0 e^{i\omega t}\right\}$, where $\mathbf{F}_0$, is the amplitude of the sinusoidal force and $\Re e\left\{...\right\}$ denotes the real part of its argument. In order to prevent the particle from wandering off from a given position, it is also subjected to a harmonic trap, $-\mathbf{H}_e \cdot \Delta\mathbf{r}_b(t)$, that allows for small excursions $\Delta\mathbf{r}_b(t)$ from the equilibrium position. Here $\mathbf{H}_e$ is the harmonic spring constant tensor $\mathbf{H}_e = \begin{bmatrix} H_{e,xx} & 0 & 0 \\ 0 & H_{e,yy} & 0 \\ 0 & 0 & H_{e,zz} \end{bmatrix}$ with zero off-diagonal components in our chosen coordinate system. Since our model polymer melt is an isotropic medium, analysis of particle motion along any direction will yield the same viscoelastic properties. In this work, we have chosen to impose the sinusoidal force along the x direction. Thus, the combined force that the particle is subjected to will be $\mathbf{f}_{ex} = \Re e\left\{\mathbf{F}_0 e^{i\omega t}\right\} - \mathbf{H}_e \cdot \Delta\mathbf{r}_b(t)$. Appropriate choice of the amplitude of the input force and the harmonic restraint parameters will ensure that the resultant oscillatory displacement along x direction will be $\langle \Delta x_b(t)\rangle = x_0(\omega)\Re e\left\{e^{i(\omega t - \phi(\omega))}\right\}$ where $x_0(\omega)$ is the amplitude of the oscillatory displacement of the particle, and $\phi(\omega)$ is the frequency dependent phase lag of the displacement with respect to the input force. In the linear regime, it is expected that $x_0(\omega) \propto F_0$ for a particular frequency ω, and the ensemble-averaged particle displacement $\langle \Delta x_b(t)\rangle$ will have contributions only at the input frequency ω (i.e. absence of higher harmonics) [48]. In this work, the following choices were made for the spring constants: $H_{e,xx} = 10$, $H_{e,yy} = 1000$ and $H_{e,zz} = 1000$. Note that, due to the use of the large values of $H_{e,yy}$ and $H_{e,zz}$, both $\langle \Delta y_b(t)\rangle$ and $\langle \Delta z_b(t)\rangle$ are negligible compared with $\langle \Delta x_b(t)\rangle$. Including these variables and parameters, we get the following expression for the friction function for active rheology:

$$Z^*(\omega) \equiv Z^*_{active}(\omega) = \frac{1}{i\omega}\left(\frac{F_0}{x_0(\omega)} e^{i\phi(\omega)} - H_{e,xx}\right). \tag{4}$$

2. Passive rheology:

For passive rheology, the friction function in Eq. (3) is given by [18]

$$Z^*(\omega) \equiv Z^*_{\text{passive}}(\omega) := \frac{6k_{\text{B}}T}{(i\omega)^2 \bar{\mathcal{F}}\left\{\left\langle \Delta\mathbf{r}_b^2(t)\right\rangle_{\text{eq}}\right\}}, \tag{5}$$

where k_B is the Boltzmann constant and $\bar{F}\{...\}[\omega]$ indicates the one-sided Fourier (or Laplace) transform of the mean squared displacement (MSD) $\langle \Delta \mathbf{r}_b^2(t) \rangle_{eq} = \left\langle [\mathbf{r}_b(t) - \mathbf{r}_b(0)]^2 \right\rangle_{eq}$ of the particle position $\mathbf{r}_b(t)$.

Eq. (3) (with $Z^*(\omega)$ given by Eq. (5)), which results from the inclusion of the medium and particle inertia in the GSER was called the inertial generalized Stokes Einstein relation (IGSER) in our previous study [18] and prior work [30, Eq. (2.17)].

III. RESULTS

A. NEMD simulations for comparison with probe rheology

Probe particle rheology results for the viscoelastic moduli will be compared with bulk rheology obtained by application of the established equilibrium and non-equilibrium MD (NEMD) simulation techniques to the same system. The equilibrium, Green-Kubo (GK) results from Sen *et al.* [49] for the bulk viscoelastic moduli of this system will be used for the purpose of the comparison. To the best of our knowledge, NEMD results of viscoelastic properties exist for short chains (N = 20), but not for this particular weakly entangled system (N = 80). We thus obtained another independent set of viscoelastic moduli values for our system by running NEMD simulations on the same model system (but without the probe particle) and at the same conditions. For these calculations, the frequency range, $\omega = 0.002$—0.08 was chosen to match the frequency range used in the probe particle rheology simulations. For a particular frequency ω, an oscillatory shear strain was imparted on the simulation box and the corresponding shear stress component was monitored as a function of time; these data were used to determine the values of $G^*(\omega)$. To capture the steady state response of the system to the shear perturbation, the first 30 (50) oscillations were discarded for the lower frequency decade (higher frequency decade). For the lower frequencies (0.002—0.01), 70 oscillations and for the higher frequencies (0.02 - 0.08), 100 oscillations were used for collecting data in these simulations. A comparison of our NEMD results with the existing literature values [49] that were obtained by the application of the Green-Kubo method to this system is shown in Fig. 1.

Over the entire frequency range we studied, the agreement between our NEMD results and the literature values [49] from the Green-Kubo method is excellent. Below we compare

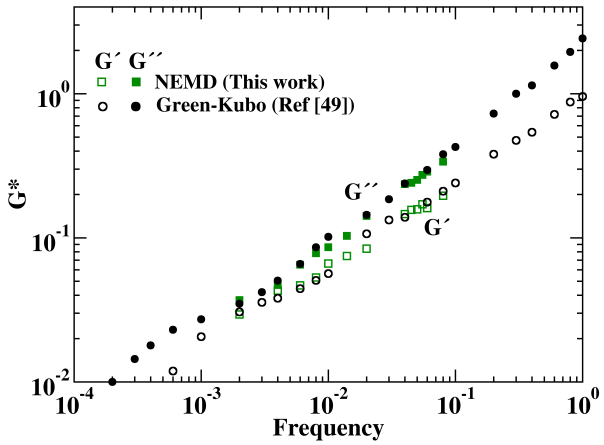

FIG. 1. (Color online) Values of the linear storage, $G'(\omega)$ (open symbols) and loss, $G''(\omega)$ (filled symbols) moduli of entangled polymer melt of chain length $N = 80$ obtained from NEMD (squares) simulations. Values are compared with the literature data (circles) obtained using Green-Kubo simulations [49].

these two sets of bulk $G^*(\omega)$ values with the $G^*(\omega)$ results obtained from the linear probe rheology simulations.

B. Probe rheology

1. *Active rheology*

In the active mode, particle motion is realized by subjecting the particle to a sinusoidal external force $\Re e\{\mathbf{F}_0 e^{i\omega t}\}$. In order to sample the linear viscoelastic regime, the force amplitude F_0 for a given frequency was selected such that the resultant oscillation magnitude $x_0(\omega)$ was much smaller than the particle diameter. It was verified that the viscoelastic modulus ($G^*(\omega)$) values so calculated were insensitive to the changes in the amplitude over this range. Another check for linearity was also performed by ensuring that the Fourier transform of the raw output oscillation signal of the particle showed only one characteristic peak—that at the forcing frequency. With this setup, simulations were performed at several frequencies over the range $\omega = 0.002$—0.1. For the lower values of frequency, i.e. $\omega = 0.002$—0.01, data for the center of mass location of the nanoparticle were collected for 80 oscillations, and for the higher frequency values, i.e. $\omega = 0.02$—0.1, these data were

collected for 100 oscillations. Out of these, data for the first 40 oscillations (equilibration stage) were discarded and the remaining values were averaged to get the time averaged sinusoidal output displacement signal. The amplitude and the phase lag of the particle oscillation were then determined from these average data by assuming the functional form $\langle \Delta x_b(t) \rangle = x_0(\omega) \Re e \left\{ e^{i(\omega t - \phi(\omega))} \right\}$. Eq. (3) with Eq. (4) was then used to calculate $G^*(\omega)$ from these simulation results.

In Fig. 2, the active probe rheology results for the viscoelastic moduli of this entangled melt are compared with our NEMD results and also the literature values that were obtained using the Green-Kubo formalism [49]. As seen from Fig. 2, the active rheology results are in good agreement with NEMD and GK results for little over a decade of frequency.

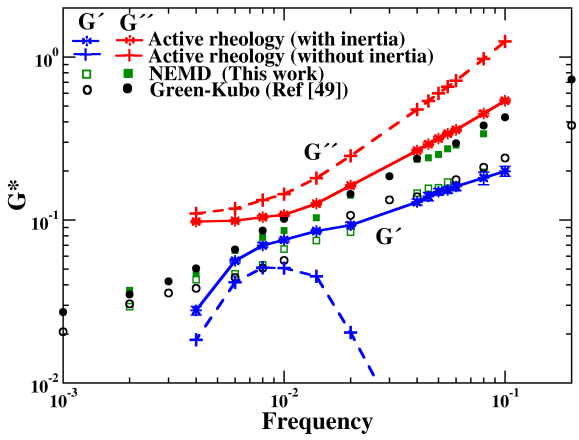

FIG. 2. (Color online) Comparison of frequency dependence of viscoelastic moduli as determined by active rheology, NEMD and Green-Kubo techniques. The upper four (solid-star, dashed-plus, filled circles and filled square) data sets are for $G''(\omega)$ and the lower four data sets (solid-star, dashed-plus, empty circles and empty squares) are for $G'(\omega)$. Solid-star lines differ from corresponding dashed-plus lines in that the former represent results obtained by accounting for medium and particle inertia while the latter represent results obtained by ignoring the medium and particle inertia in the analysis procedure. Uncertanties are shown on the results that were obtained by accounting for inertia; these were estimated by using the blocking method [50].

Fig. 2 also presents a comparison of $G^*(\omega)$ values calculated with and without accounting for the medium and particle inertia. As was also observed in our previous work on an unentangled polymer melt system [18], the $G'(\omega)$ (dashed-plus line in Fig. 2) exhibits

negative values at higher frequencies when the medium and particle inertia are not included in the analysis. This observation can be attributed to the importance of both the Basset and the added mass acceleration terms at the higher frequencies. This effect is further amplified by the use of the larger particle in the present study. Inclusion of the inertial effects in the analysis not only removes these negative $G'(\omega)$ values at high frequencies but also substantially enhances the agreement between the active probe rheology results and the results from the NEMD and the Green-Kubo techniques. As was the case for the unentangled polymers [18], this observation of ours for the entangled system also is opposite to that of Kuhnhold and Paul [38] who found that when inertia was not accounted for in the analysis, the storage modulus continued to exhibit positive values, whereas accounting for the inertia in their analysis led to unphysical values for the storage modulus in many instances. Fig. 2 further shows that at lower values of frequencies, the $G'(\omega)$ shows a stronger decrease than that observed in NEMD or Green-Kubo results, while the $G''(\omega)$ attains a plateau value even after including medium and particle inertia in the analysis of active rheology simulations. We attribute this artifact to the hydrodynamic interactions between the periodic images of the moving particle in the simulations; a more detailed discussion of this effect is presented below.

2. Passive rheology

In this simulation, the probe particle was allowed to move through the entangled melt under the influence of thermal fluctuations. Ten independent system replicas were used and in order to capture the different regimes of particle motion, the particle trajectory was tracked over as long a time scale (more than 500 million MD time steps) as practically possible given the current computational power. In Fig. 3, we show the time dependence of the mean-squared displacement (MSD) of the nanoparticle obtained by averaging over 10 replicas. The MSD shows 3 regimes: a short time scale ballistic regime, an intermediate transient regime related to local caging (see inset in Fig. 3), and a "diffusive-like" regime at long times. The statistical inaccuracies at these longer time scales are also seen from the inset in Fig. 3. At longer times, approximately $t \gtrsim 5 \times 10^5$, the plot of MSD vs. time on the log scale has a slope of 0.93, thus indicating that the particle motion approached, but did not reach, the diffusive regime, even at these long simulation times. In our previous study

for an unentangled polymer melt system [18], we were able to capture the diffusive regime over the simulation time scale. However, this higher-molecular weight system exhibits longer relaxation times, which makes obtaining good statistics in the terminal zone more expensive. One could perhaps sample the true diffusive regime for this system by tracking the probe

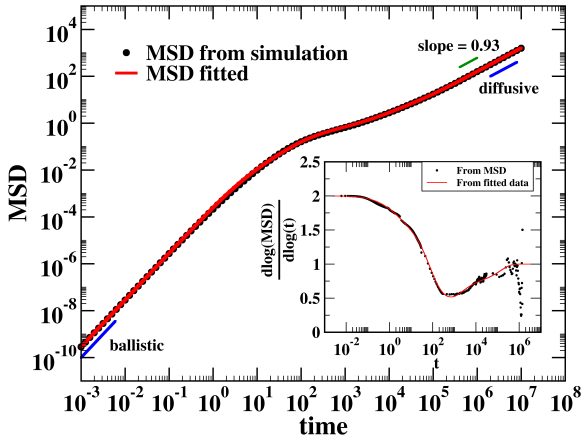

FIG. 3. (Color online) Averaged MSD (black dots) of a probe particle from 10 independent replicas. Solid red line is the fitting curve obtained by Eq. 6 with $\alpha_1 = 2.807$, $\alpha_2 = 1.877$, $\alpha_3 = 0.2111$, $\alpha_4 = 0.7933$, $\tau_0 = 0.08$, $\tau_1 = 1.6$, $\tau_2 = 37$, $\tau_3 = 600$, $\tau_4 = 150000$ ($\chi^2 = 0.0086$). Inset shows the logarithmic slope of MSD with respect to time (calculated using Euler differencing approach) where a transient caging effect due to the entangled mesh is evident from the minimum in the slope.

motion over a longer period of time, may be one or two more time decades. But due to the practical limitations in the current computational power, such long time simulations are not presently feasible. For this reason, we have restricted these simulations to the longest timescale practically achievable with current computational resources.

We have used an analytical fitting procedure to the MSD to capture the different regimes of particle motion from the ballistic to the diffusive; the analytical expression is then used in the IGSER, Eq. 3, to determine $G^*(\omega)$. For this purpose, we used two analytical functions (Eqs. 8 and 9 below) which can capture both the short time ballistic regime and the long time diffusive regime. This analytical fitting procedure is briefly summarized here. Specifically, in single probe microrheological analysis, usually the logarithm of the MSD is fit to a polynomial of $\ln t$, and then an approximate expression of the one-sided Fourier

(or Laplace) transformation is used for the polynomial to derive $G^*(\omega)$ from the MSD via GSER [13, 28]. This method is practically useful but the approximation for the Laplace transformation is poor when the MSD's slope varies rapidly, and also the physical meaning of the values of fitting parameters (i.e. the coefficient of the each order term and the order of the polynomial) is lost. To overcome these limitations, we proposed a more accurate and physically intuitive method [18] that utilizes the power-law spectrum used for the analysis of viscoelastic relaxation spectrum [51]. In this scheme, the MSD is expressed as

$$\left\langle \Delta \mathbf{r}_b^2(t) \right\rangle_{\mathrm{eq}} = \int_0^\infty f^{(1)}(t,\tau)\frac{h(\tau)}{\tau}d\tau + g_0 f^{(0)}(t,\tau_{\max}), \tag{6}$$

The spectrum is given by

$$h(\tau) = \sum_{j=1}^{n_{\max}} g_j \tau^{\alpha_j} H(\tau_j - \tau) H(\tau - \tau_{j-1}), \tag{7}$$

where n_{max} is the total number of modes of the spectrum, τ_j and α_j are the relaxation time and the exponent for the jth mode ($\tau_j > \tau_{j-1}$) respectively, and $H(\tau)$ is a unit Heaviside function. Hereafter we denote $\tau_{n_{\max}}$ as $\tau_{\max}$ for simplicity. The weight function in front of the spectrum was introduced to guarantee that the MSD exhibits ballistic behavior $\left\langle \Delta \mathbf{r}_b^2(t) \right\rangle_{eq} = Ct^2$ in the smallest time regime $t \ll \tau_0$

$$\begin{aligned} f^{(1)}(t,\tau) &= 1 - (1 + t/\tau)e^{-\frac{t}{\tau}} \\ &\approx \begin{cases} t^2/(2\tau^2), & \text{for} \quad t \ll \tau \\ 1, & \text{for} \quad t \gg \tau \end{cases} \end{aligned} \tag{8}$$

On the other hand, the second term with the function

$$\begin{aligned} f^{(0)}(t,\tau_{\max}) &= e^{-t/\tau_{\max}} - 1 + t/\tau_{\max} \\ &\simeq \begin{cases} t^2/(2\tau_{\max}^2), & \text{for} \quad t \ll \tau_{\max} \\ t/\tau_{\max}, & \text{for} \quad t \gg \tau_{\max} \end{cases} \end{aligned} \tag{9}$$

was added to ensure that the MSD shows the diffusive behavior $\left\langle \Delta \mathbf{r}_b^2(t) \right\rangle_{eq} = 6\mathcal{D}t$ in the longest time regime $t \gg \tau_{\max}$. The second term on the right-hand side of Eq. (6) must be equal to first term at $t = \tau_{\max}$ for the MSD to be diffusive when $t \gg \tau_{\max}$ [52]. This requirement determines the weight of the second term as $g_0 = \sum_{j=1}^{n_{\max}} g_j \left(\tau_j^{\alpha_j} - \tau_{j-1}^{\alpha_j}\right)/\alpha_j$. Also, by imposing continuity for the weighting of the modes, the weight g_1 of the first mode determines

the rest as $g_j = g_1 \prod_{k=1}^{j-1} \tau_k^{\alpha_k - \alpha_{k+1}}$ for $2 \le j \le n_{\max}$. Furthermore, the first weight is related to the coefficient of the ballistic motion by $C = \frac{g_1}{2} \sum_{j=1}^{n_{\max}} \left(\prod_{k=1}^{j-1} \tau_k^{\alpha_k - \alpha_{k+1}} \right) \frac{\tau_j^{\alpha_j - 2} - \tau_{j-1}^{\alpha_j - 2}}{\alpha_j - 2} + \frac{g_0}{\tau_{\max}^2}$. (Usually the last term can be neglected safely because $\tau_{\max}$ is large.) Therefore once C is estimated from the initial slope of the MSD data on the log-log scale independent of the fitting, g_1 can be obtained from the other parameters through this relation. Summarizing, for a given $n_{\max}$, the number of free adjustable parameters $\{\alpha_1, ..., \alpha_{\mathrm{mx}}, \tau_0, ..., \tau_{\max}\}$ is $2n_{\max}+1$ in total ($\alpha_{\max} := \alpha_{n_{\max}}$) [52]. We assign approximately one mode per decade of time for the time window except the ballistic and diffusive regimes, and assume $n_{\max} = 4$ as in the previous study [18].

It is important to note that the expression of the MSD, Eq. (6), is analytically Laplace transformed. If Eq. (8) and (9) are substituted into Eq. (6) and then the integration is conducted with respect to τ, one obtains

$$\left\langle \Delta \mathbf{r}_b^2(t) \right\rangle_{\mathrm{eq}} = \sum_{j=1}^{n_{\max}} g_j \left[\tau^{\alpha_j} \left(1/\alpha_j - e^{t/\tau} + (\alpha_j - 1) E_{1+\alpha_j}(t/\tau) \right) \right]_{\tau=\tau_{j-1}}^{\tau=\tau_j} + g_0 \left(e^{-t/\tau_{\max}} - 1 + t/\tau_{\max} \right) \tag{10}$$

where $E_{1+\alpha}(t/\tau) = \int_1^\infty dx\, x^{-1-\alpha} e^{-xt/\tau}$ is the exponential integral function. Therefore the real and imaginary parts of $\bar{\mathcal{F}} \left\{ \langle \Delta \mathbf{r}_b^2(t) \rangle_{eq} \right\} = r'(\omega) + i r''(\omega)$ are obtained as

$$r'(\omega) = -2 \sum_{j=1}^{n} \frac{g_j}{1+\alpha_j} \left[\tau^{1+\alpha_j} {}_2F_1 \left(2, \frac{1+\alpha_j}{2}; \frac{3+\alpha_j}{2}, -\tau^2\omega^2 \right) \right]_{\tau=\tau_{j-1}}^{\tau=\tau_j} - \frac{g_0}{\tau_{\max}\omega^2 (1 + \tau_{\max}^2 \omega^2)}, \tag{11a}$$

$$r''(\omega) = -\frac{1}{\omega} \sum_{j=1}^{n} \frac{g_j}{\alpha_j (\alpha_j + 2)} \left[\tau^{\alpha_j} \left\{ 2 + \alpha_j - \alpha_j \tau^2 \omega^2 {}_2F_1 \left(1, 1 + \frac{\alpha_j}{2}; 2 + \frac{\alpha_j}{2}, -\tau^2\omega^2 \right) \right. \right. \left. \left. - 2\alpha_j \tau^2 \omega^2 {}_2F_1 \left(1, 1 + \frac{\alpha_j}{2}; 2 + \frac{\alpha_j}{2} - \tau^2\omega^2 \right) \right\} \right]_{\tau=\tau_{j-1}}^{\tau=\tau_j} - \frac{g_0}{\omega (1 + \tau_{\max}^2 \omega^2)}, \tag{11b}$$

where ${}_2F_1$ is the hypergeometric function, and $[f(\tau)]_{\tau=x}^{\tau=y} := f(y) - f(x)$ for an arbitrary function $f(\tau)$. We find the parameters $\{\alpha_1, ..., \alpha_{max}, \tau_0, ..., \tau_{\max}\}$ as follows. First we fix the relaxation times $\{\tau_i\}$, and then numerically seek exponents $\{\alpha_i\}$ that minimize χ^2 of $-\ln(MSD)$ within a certain window of $\{\alpha_i\}$ for the fixed $\{\tau_i\}$ (the appropriate values of $\{\tau_i\}$ and the center of the window $\{\alpha_i\}$ are estimated by manual fitting). It is important to choose an appropriate window width to attain high accuracy of fitting because in practice the minimization is attainable only locally in the parameter space, due to the nonlinear

nature of Eq. (6) with respect to these parameters. We compare the minimized χ^2 value to that obtained from the conventional method based on least-square fitting of the polynomial function of $\ln t$ (with order 7∼10). If our value of χ^2 is much larger than the conventional one, we modify $\{\tau_i\}$ or the window of $\{\alpha_i\}$ so that we can get χ^2 smaller than, or at least comparable to, the conventional one to guarantee that our fitting is almost as accurate as the conventional method. The fitted line obtained by this procedure is shown in Fig. 3. We then calculate $G^*(\omega)$ by using Eqs. (10–11), and IGSER, Eq. (3) for the thus-obtained parameter values. This calculation of $G^*(\omega)$ can be done without the approximation typically used, and is superior to the conventional method for the accuracy of the inverse Laplace transformation. But it should be noted that our method takes more effort for fitting the MSD compared to the conventional least-square fitting of the polynomial function.

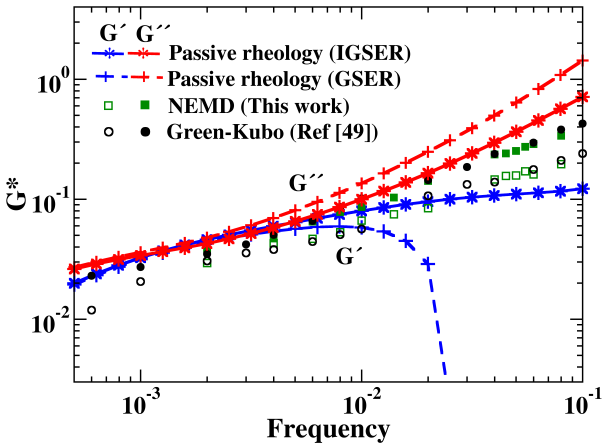

FIG. 4. (Color online) Comparison of the $G^*(\omega)$ values obtained by passive probe rheology, NEMD and Green-Kubo techniques. The upper red solid star and red dashed plus lines represent $G''(\omega)$ and the lower blue solid star and blue dashed plus lines represent $G'(\omega)$ values obtained probe rheology. For the NEMD and Green-Kubo values, the open symbols denote $G'(\omega)$ while the solid symbols denote $G''(\omega)$.

Fig. 4 shows a comparison of the passive probe rheology results that were obtained by considering (i.e. using IGSER) and ignoring (i.e. using GSER) the medium and particle inertia with our NEMD results as well as with the literature Green-Kubo values [49]. For the weakly entangled melt studied here, $G'(\omega)$ values are always smaller than the $G''(\omega)$ values indicating that the melt shows predominantly liquid-like behavior over the frequency range

studied in this work. The $G^*(\omega)$ values obtained from passive probe rheology by applying GSER (i.e. by ignoring the medium and particle inertia) in the analysis (dashed lines in Fig. 4), show a large disagreement with the corresponding values obtained from NEMD and Green-Kubo methods over the entire frequency range. In fact, at higher frequencies ($\omega \geq 10^{-2}$), the $G'(\omega)$ obtained from such an exercise becomes unphysically negative. Indeed, the $G'(\omega)$ values obtained by the inclusion of medium and particle inertia in the analysis (i.e. by applying IGSER) are no longer negative. The agreement between the $G^*(\omega)$ values obtained from probe rheology with NEMD and Green-Kubo methods is improved in this case, and is of comparable quality to the active probe rheology approach. The $G^*(\omega)$ values from probe rheology exhibit larger deviations from other methods at both ends of the frequency range, which can be explained as follows. At the higher values of frequency ($\omega \gtrsim 10^{-1}$), the motion of the particle becomes ballistic and thus MSD values in this regime cannot be used for determining the material viscoelastic properties. As was also mentioned for active rheology, the artifactual hydrodynamic intreactions between the periodic images of the probe particle affect results at the lower end of the frequency range; this effect is discussed in details below.

IV. DISCUSSION

A. Effect of probe particle size

The applicability of probe particle rheology to an entangled polymer system is governed by the interplay of several characteristic length scales: the monomer segment size (d), the chain radius of gyration (R_g), the entanglement tube diameter (d_T), and finally, the wavelength (Λ) and the penetration depth (Δ) of shear waves. The latter effects are described in the next sub-section.

Most synthetic polymers are flexible, for which $d < d_T \ll R_g$. The application of continuum mechanics relations for analyzing simulation data implicitly assumes that the probe particle size is significantly larger than the characteristic size of the molecules of the medium i.e. $R > R_g$ and also that $R \gg d_T$ [26, 53]. At the other end of the scale, it was shown in experiments that nanoparticle diffusion is much faster (∼200 times) than that predicted by the Stokes-Einstein relation when the particle radius is smaller than the tube diameter [54, 55]. In this regime ($R < d_T$), particle motion through the polymer matrix does not de-

pend on the disentanglement of the chains, but rather depends on the local rearrangements of the chain segments on the length scales below d_T, where the chain segments do not feel the presence of entanglements [29, 54, 55]. As a result, the particle no longer probes the continuum properties of the medium, but rather one observes a microscopic response to a specific probe.

For heavily entangled melts (degree of entanglement or average number of entanglements per chain, $\langle Z \rangle_{\rm eq} > 4$), theoretical work by Yamamoto and Schweizer [26] predicted the recovery of Stokes-Einstein diffusion when $R/d_T \gtrsim 5$. Similarly, experimental work on well entangled DNA solutions [56] found probe rheology results to be consistent with continuum mechanics at $R \gtrsim 3d_T$. It should be kept in mind that estimates of d_T are model dependent

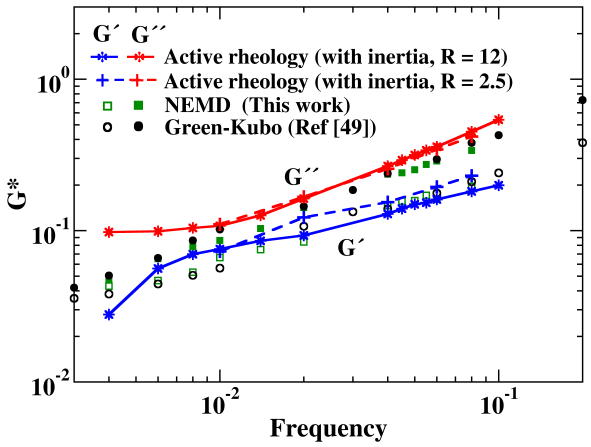

FIG. 5. (Color online) Comparison of active probe rheology results for two different particle sizes, R =2.5, and 12.0. The upper two curves along with the filled symbols are for $G''(\omega)$ and the lower two curves along with the open symbols are for $G'(\omega)$.

[57], and may vary by a factor of two. In our work, we have used a particle of nominal radius $R = 12$, for our weakly entangled polymer melt system ($\langle Z \rangle_{\rm eq} \sim 1.5-2$) whose entanglement distance has been reported in the literature [58] to be $d_T \approx 7.7$. Thus, for our system, the ratio of R/d_T is 1.56, which is smaller than both the literature studies mentioned above [26, 56]. Yet, as described above, over the frequency range of applicability of our technique, the probe rheology results are in agreement with the Green-Kubo and NEMD values of the medium viscoelasticity.

To further judge the effect of the choice of the particle size on our probe rheology results,

we performed active rheology calculations with a smaller particle ($R = 2.5$) over the frequency range $0.01 < \omega \leq 0.08$. As seen in Fig. 5, $G''(\omega)$ obtained from the smaller particle shows good agreement with that obtained from the larger particle. The values of $G'(\omega)$ obtained by the use of different sized particles also show agreement though the differences are larger than those for $G''(\omega)$. Note that we performed the comparison using only the active rheology technique since this is a much faster calculation than passive rheology. In principle, the test of particle-size dependence should also include calculations with a particle of size $R \sim 40$ (i.e. $R/d_T > 5$). The shear wave propagation effects (discussed in the next subsection) would become even more prominent in such a case, and their mitigation would necessitate use of much larger simulation boxes than that used here, making such a calculation impractical at the current time.

B. Penetration depth and shear wave propagation effects

For active particle rheology (Fig. 2), storage and loss moduli [$G'(\omega)$ and $G''(\omega)$] estimations deviate from the NEMD and the Green-Kubo values at frequencies $\omega \lesssim 0.008$. Similarly, the agreement between passive rheology (Fig. 4), on the one hand, and the NEMD and Green-Kubo results on the other, also suffers in the same frequency range. We attribute these artifacts to shear wave propagation effects in the 3D periodic simulation system that were discussed in our previous work [18]. The possibility of the occurrence of these effects can be judged by focusing on two length scales associated with the propagating wave—the wavelength Λ and the penetration depth Δ of the wave in the medium. For a viscoelastic fluid, these length scales are given by $\Lambda(\omega) = \frac{|G^*(\omega)|}{\omega}\sqrt{\frac{2}{\rho}\frac{1}{|G^*(\omega)|+G'(\omega)}}$, and $\Delta(\omega) = \frac{|G^*(\omega)|}{\omega}\sqrt{\frac{2}{\rho}\frac{1}{|G^*(\omega)|-G'(\omega)}}$ [33] as shown in Fig. 6. These were estimated by using $G^*(\omega)$ from the Green-Kubo technique [49], since $G^*(\omega)$ values calculated from probe rheology could be affected by the shear-wave propagation phenomena at both ends of the frequency range. The minimum distance between the surfaces of the nearest images of the moving particles in our simulation system is $l \approx 150 - 25 \approx 125$ and is shown by the upper horizontal line in Fig. 6. Thus, for frequencies $\omega \lesssim 0.005$, the penetration depth of the shear wave will be larger than the minimum distance between the nearest neighbor particles—i.e., the shear wave propagating from a moving particle will affect the motion of its six closest neighbor particles in our system, and vice versa. These interactions are not accounted for in our

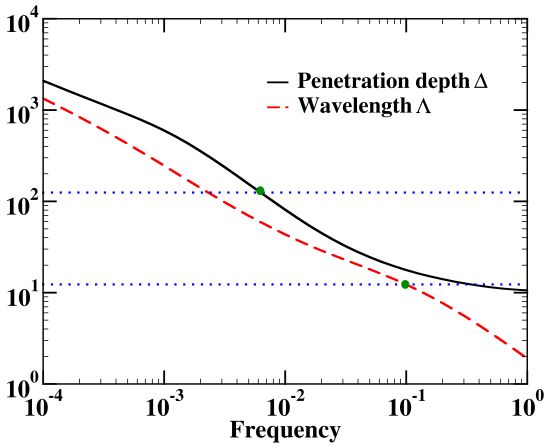

FIG. 6. (Color online) Frequency dependence of the penetration depth (solid black line) and the wavelength (dashed red line) of the propagating shear wave calculated using the literature Green-Kubo values. The minimum distance between the moving probe particle and its images (upper) and the probe particle size (lower) are shown by horizontal (dotted blue) lines.

continuum analysis, so that the moduli values calculated from the IGSER expression are unreliable at these frequencies.

As the plot of penetration depth versus frequency shows, the problem is worst at low frequencies. Assuming one wishes to retrieve the dynamic modulus down to frequencies in the terminal zone, near the low-frequency crossover in the dynamic modulus, a simple scaling estimate can be made for the necessary box size for this purpose. In the terminal zone, the liquid behaves nearly Newtonian, and the storage modulus can be neglected. Hence, the penetration length is the Newtonian one: $\Delta \cong \sqrt{\frac{2\eta_0}{\rho\omega}}$, where η_0 is the zero-shear rate viscosity, and can be estimated as $\eta_0 \cong G_N^0 \tau_d$. For entangled polymers, the plateau modulus $G_N^0 \cong \rho k_{\rm B} N_{\rm A} T/M_e$ (where $N_{\rm A}$ is the Avogadro number) is independent of molecular weight, and the longest relaxation time goes as [59] $\tau_d \cong \frac{\tau_e}{40}(M_w/M_e)^{7/2}$, where τ_e is the strand relaxation time, approximately the inverse of the frequency at the high-frequency crossover of the dynamic modulus. We are interested in frequencies $\omega \gtrsim 1/\tau_d$, so the maximum penetration length is $\Delta_{\rm max} \cong \frac{1}{40}\sqrt{\frac{2k_{\rm B}N_{\rm A}T}{M_e}}\left(\frac{M_w}{M_e}\right)^{7/2}\tau_e$. Our simulation box must be significantly larger than this size, which may be compared to the radius of gyration of the polymer $R_g \cong \frac{\sqrt{M_w}a_{\rm K}}{\sqrt{6M_{\rm K}}}$, where $a_{\rm K}$ is the Kuhn step length and $M_{\rm K}$ is the Kuhn step

molecular weight. Hence, we find

$$\frac{\Delta_{\max}}{R_g} \cong \sqrt{\frac{12 k_{\mathrm{B}} N_{\mathrm{A}} T}{M_{\mathrm{K}}}} \frac{\tau_e}{a_{\mathrm{K}}} \frac{\langle Z \rangle_{\mathrm{eq}}^3}{40 N_e}, \tag{12}$$

where $N_e = M_e/M_{\mathrm{K}}$ is the average number of Kuhn steps in an entanglement and $\langle Z \rangle_{\mathrm{eq}} = M_w/M_e$ is the average number of entanglements per chain. In other words, a naïve estimate of the minimum box size that considers only polymer size, and neglects the hydrodynamic interaction of the particle with its images grows worse with the number of entanglements (Z) cubed.

However, not only the scaling but also the prefactor is important. As an example, we consider polystyrene at $T = 180°\mathrm{C}$, where $M_{\mathrm{K}} = 726\mathrm{Da}$ [60], $a_{\mathrm{K}} = 1.5\mathrm{nm}$ [61], $N_e \cong 15$ [62], and $\tau_e \cong 1\mathrm{ms}$ [59], we find $\frac{\Delta_{\max}}{R_g} \cong 2.8 \times 10^5 \langle Z \rangle_{\mathrm{eq}}^3$. For this system, the box needs to be at least 5 orders of magnitude larger than expected using the naïve calculation.

Estimates of the box size required for capturing the terminal zone for the bead-spring model considered in this work can also be made. Thus, using values of $\eta_0 = 55$ and $\omega = 1 \times 10^{-4}$ from the Green-Kubo results [49] in the expression $\Delta \cong \sqrt{\frac{2\eta_0}{\rho\omega}}$, we obtain an estimate of $\Delta_{\max} \cong 1138$ i.e. $\frac{\Delta_{\max}}{R_g} \cong 257$, where we have used a value of $R_g = 4.42$ for our model chains. Thus, even for the lightly entangled model system studied here, viscoelasticity in the terminal region can only be captured in probe rheology simulations if boxes of size greater than 1150 (i.e. about 250 times the chain size) are used. These would be very large systems for simulations, keeping in mind that the number of beads in the system scales as the cube of the box size.

Rather than using such large systems, a better approach would be to capture the wave propagation effects in the analysis methodology by including the multibody hydrodynamic interactions along with the inertial contributions in the force balance, this is an involved task and beyond the scope of the current work. Furthermore, it appears that the repeated and forced creation of the propagating wave in the active mode leads to a stronger wave than the stochastically created wave in the passive mode, in turn, leading to a stronger effect of the multibody hydrodynamic interactions between the images of the probe particle in active mode. An investigation of this effect should also be a part of the future work in this field.

At the other end of the frequency range studied (i.e. at $\omega \geq 0.1$), the wavelength of the shear wave becomes smaller than the particle size. Physically, the Basset force starts becoming dominant over the Stokes drag [33] at these frequency values. The particle motion

is predominantly ballistic (and hence independent of the medium viscoelasticity) in this regime, thus making it difficult to extract the medium viscoelastic properties by the analysis of the particle motion [18]. This effect is clearly seen from the significant disagreement between the passive rheology results and the NEMD or Green-Kubo values in this frequency range, the active rheology calculations were not attempted in this frequency range.

In summary, the wave propagation effects put restrictions on the frequency range over which viscoelasticity can be investigated via probe rheology methods. In simulations, box sizes are often picked in relation to the size of the molecule or the probe particle studied, our analysis demonstrates the need for considering the range of the hydrodynamic interactions when selecting a box size for determining the viscoelasticity over a given frequency range by probe rheology simulations.

C. Deduction of particle displacement from medium viscoelasticity data

In many practical applications involving, for example, nanoparticle-based drug delivery to tumors [63, 64], the quantity of central interest is the nanoparticle motion in a given complex medium on different time scales. Such information can be used for deducing the penetration depth to which the diffusing particle such as the drug carrying nanoparticle will travel in the medium over a certain time scale. The IGSER described above provides a transform between the particle MSD and the medium viscoelastic properties. Thus, in principle, IGSER can be applied in the reverse direction to determine the particle MSD over a given time scale from the knowledge of the viscoelastic spectrum of the complex medium.

To assess the ability of the IGSER to predict the particle motion in the entangled polymeric melt from its viscoelasticity, we used G^* that Sen *et al.* [49] calculated based on the Green-Kubo approach. We point out here that their G' and G'' data at high frequencies are almost parallel, and also the slope in the log-log scale is very close to 2/3. The same tendency is observed in our NEMD result (see Fig. 1) and also in the simulations of unentangled chains by Cifre *et al.* [65]. Thus surprisingly, G^* at the high frequencies is well described by the Zimm model [66] rather than the Rouse model, indicating that the hydrodynamic interactions between polymers are not screened out. Also, the overall G^* fits very well with a combination of the Zimm model and the two-mode Maxwell model (see inset of Fig. 7). Using this approach, we converted G^* into the MSD by using the IGSER given by Eq. (3)

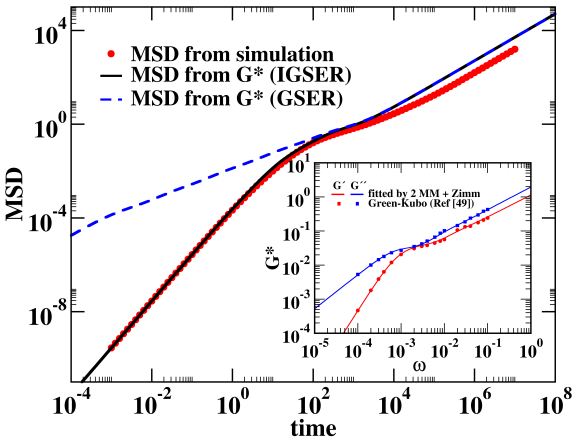

FIG. 7. (Color online) Comparison of the probe particle MSD measured in the passive rheology simulations (dotted) and that predicted from literature G^* values [49] (shown in inset). Solid line is derived from the IGSER whereas dashed line is from the conventional GSER. In inset, solid lines are fitting curves by a superposition of the Zimm model (with the relaxation time 20 and the amplitude 0.12) and the 2-mode Maxwell model (with the relaxation times $\{1100, 65\}$ and the amplitudes $\{0.038, 0.065\}$).

along with Eq. (5); a comparison of the result with the probe particle MSD measured in the passive rheology simulations is shown in Fig. 7. As seen from the figure, we obtain excellent agreement between the two over several decades in time except the long-time diffusive regime ($t > 10^3$). The disagreement in the diffusive regime is the counterpart of the difference in G^* at the terminal flow regime (see Fig. 1). Probably this disagreement is due to larger statistical errors from shorter simulation times in the Green-Kubo approach of the G^* calculation as we have shown for unentangled polymeric melt in the previous paper [18]. On the other hand, the agreement in the MSD in the ballistic regime is not surprising because the MSD is not affected by G^* of the medium in this short time regime: that is, no matter what the G^* is, the MSD is given by $\langle \Delta r_b^2(t) \rangle = \frac{3k_{\rm B}T}{m_{\rm observed}} t^2$ [18]. If we use the conventional GSER without inertial effects (see dashed curve in Fig. 7), then the MSD predicted from G^* does not agree with that measured in the passive rheology simulations neither in the short time ballistic and Basset regimes (due to absence of inertia in the analysis) nor in the long time regime (for the same reasons as for IGSER i.e. statistical errors in Green-Kubo approach at longer times).

D. Added mass of the medium

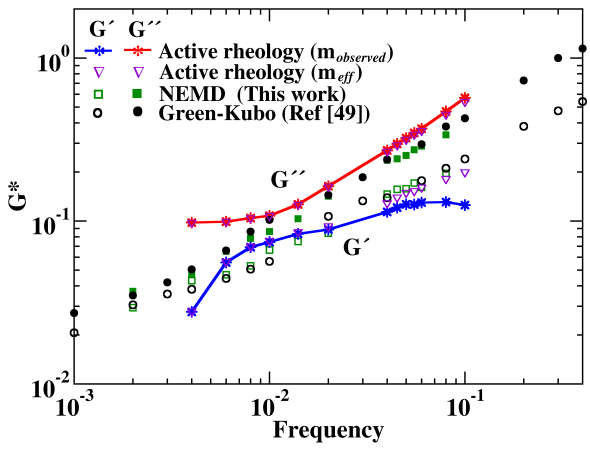

FIG. 8. (Color online) Comparison of active rheology results obtained by considering the probe particle mass to be $m_{\text{observed}} = 10,500$ and $m_{\text{eff}} = 13,500$. The results from NEMD simulations and literature Green-Kubo calculations are also shown.

In our previous work on an unentangled system [18], we had shown that the "observed" particle mass (*i.e.*, the mass value obtained from the particle motion in the ballistic regime) rather than the "effective" mass (*i.e.,* the mass value obtained by considering the mass of the medium dragged with the particle), is to be used in the application of the continuum analysis to the simulation data. That observation was explained by demonstrating that the calculated shell thickness of the polymer mass moving with the probe (i.e. the added mass) was smaller than the polymer bead size which was the smallest length scale in that system [18]. To study this aspect for the current system, we calculated the observed mass of the probe using the same procedure as described in our previous study [18]—*i.e.,* by fitting the ballistic regime of MSD. In this regime $\langle \Delta r_b^2(t) \rangle = Ct^2$, the constant $C = \frac{3k_bT}{m_{\text{observed}}}$ can be determined by taking the limit, $\lim_{t\to 0} \langle \Delta r_b^2(t) \rangle / t^2$ of our simulation MSD data. This exercise yields a value of $m_{\text{observed}} = 10,500$. Per continuum mechanics, the effective mass of the probe is obtained by including the mass of the medium that is considered to be moving with the probe as given by: $m_{\text{eff}} = m_{\text{bare}} + m_{\text{add}} = 10,100 + \frac{2}{3}\pi R_H^3 \rho = 13,500$. Thus, m_{observed} is smaller than m_{eff} but larger than the bare particle mass, m_{bare}.

The viscoelastic properties obtained by considering the observed and effective particle masses for active rheology are compared against the values from the NEMD and Green-

Kubo techniques in Fig. 8. As seen from the figure, the use of m_{observed} results in larger deviations of the calculated moduli values (specifically G' values) from those obtained using the NEMD and Green-Kubo techniques, especially at higher values of frequency. This observation suggests that m_{eff} is the appropriate mass to be used in the continuuum analysis for the system studied here. The difference in the behavior from the previous work can be explained as follows. If the added mass of the polymer melt that is moving with the probe nanoparticle during its unsteady motion is considered to reside in a fluid shell around it, the shell thickness L_S, can be estimated as $\frac{2}{3}\pi R_H^3 \rho = \frac{4}{3}\pi \left((R_H + L_S)^3 - R_H^3 \right) \rho$. For the system used in the current study, this yields a value of $L_S = 1.78$ which is larger than the smallest length scale in the system i.e. monomer size = 1. On the other hand, for the particle used in the previous work ($R_H = 2.82$) [18], the shell thickness so calculated ($L_S = 0.41$) was smaller than the monomer size, thus violating the continuum treatment of the medium.

V. CONCLUSIONS

We have applied the probe particle rheology simulation technique in both active and passive modes to determine the viscoelastic properties of a lightly entangled polymer melt system. For the passive mode, we find that, in spite of conducting extremely long simulations by contemporary simulation standards for systems of this size, the "true" diffusive regime of the probe particle motion still could not be captured in the simulations. Nevertheless, we fitted the MSD data to an analytical functional form that gives the correct MSD behavior in both short (ballistic motion) and long (diffusive motion) time regimes, this analytical form was used to obtain the moduli values from the passive rheology approach. Similar to our previous work for an unentangled polymeric system, we show that for the entangled system studied here, the inclusion of the particle and medium inertia in the continuum analysis leads to good agreement between the viscoelastic properties obtained by probe rheology and those obtained from the established simulation approaches, namely the Green-Kubo and the NEMD methods. Our observation is in contrast to recent work [38] which concluded that it was not possible to judge which of the different mathematical variants used for including inertial effects in probe rheology lead to the correct values of the medium viscoelasticity.

Another important contribution of this work is we show that if the viscoelastic spectrum of the complex medium is available then the IGSER can be used to predict nanoparticle

displacement in the medium over the time scale of interest. Such ability could be of interest for applications involving nanoparticle diffusion, where it might be easier to measure the medium viscoelasticity rather than tracking the particle motion over a long time.

In addition to the significantly longer relaxation times, the entangled system presents other complexities, such as the presence of one more length scale, namely, the entanglement length scale. For the continuum Stokes treatment to be applicable, previous work suggests that for heavily entangled polymers, the moving particle should satisfy $R/d_T \gtrsim 3-5$. This requirement would necessitate use of a particle of size $23 \sim 38$ requiring even longer simulations and larger simulation boxes to mitigate the effects from shear wave propagation. Given the practical limitations of computational power, the actual simulations were performed with a particle of nominal radius $R = 12$ ($R/d_T \sim 1.5$). With this particle size, our results for the probe rheology are in good agreement with those from NEMD and Green-Kubo techniques. Surprisingly, test simulations carried out with a probe particle of size $R = 2.5$ (i.e. $R/d_T \sim 0.32$), also gave effectively the same moduli values as those obtained from the simulations with the particle of size $R = 12$. Apparently, our lightly entangled system shows less sensitivity to probe size than what is predicted in the literature.

The frequency range over which the probe rheology simulation technique is applicable is determined by considering the shear wave propagation effects. The lower bound of this frequency range is set by the hydrodynamic interactions between the periodic images of the moving particle. We derived a simple expression to estimate how much larger this penetration length is than the radius of gyration. We found that this ratio scales with the entanglement number cubed. Moreover, the prefactor can be very large for real systems. In order to avoid system-size related artifacts, a common practice in molecular simulations is to choose a box size based on the considerations of molecule (or probe) size and the length scale of the interbead interactions. Our work shows that the hydrodynamic interactions, however, are much longer range than the interparticle interactions, and as a consequence of this, much larger box sizes are required for the simulations of phenomena such as probe rheology that involve significant hydrodynamic interactions. In principle, this effect could be included in the continuum analysis by explicitly accounting for the multibody hydrodynamic interactions along with the inertial effects. Future work in this direction would help extend the range of the technique to lower values of the frequency without necessitating the use of very large simulation systems.

One advantage of experimental probe rheology is the requirement of very small amount of sample which is valuable when the sample is scarce or expensive. For computations, sample size requirements for probe rheology, NEMD and Green-Kubo techniques are similar. Our analysis has shown that long range hydrodynamic interations put restrictions on the frequency range that can be investigated in probe rheology. Thus, the frequency range over which probe rheology can be applied is comparable to that for Green-Kubo technique and is smaller than that for NEMD. As discussed, this frequency range for probe rheology can be expanded by adding multibody hydrodynamics to the analysis. One potential advantage of particle rheology is that the technique is capable of probing local rheology whereas NEMD and Green-Kubo techniques can only yield overall or effective values of the medium viscoelasticity. From the experimental point of view, the IGSER formalism has the ability to predict nanoparticle motion in complex soft matter from the knowledge of medium viscoelasticity, this will be useful in applications such as drug delivery where experimentally measuring viscoelasticity of the medium is a simpler task than tracking 3-dimensional particle motion in the medium.

Acknowledgments: MK and RK acknowledge the Texas Advanced Computing Center (TACC) at The University of Texas at Austin for providing high-performance computing resources that have contributed to the research results reported within this paper. JDS and TI acknowledge financial support from DARPA through grant W911NF-09-1-0378 and the Army Research Office, through grant W911NF-11-2-0018 and thank A. Córdoba for insightful discussions.

[1] T. A. Waigh, Rep. Prog. Phys. **68**, 685 (2005).

[2] T. M. Squires and T. G. Mason, Annu. Rev. Fluid Mech. **42**, 413 (2010).

[3] N. Gal, D. Lechtman-Goldstein, and D. Weihs, Rheologica Acta **52**, 425 (2013).

[4] T. G. Mason and D. A. Weitz, Phys. Rev. Lett. **74**, 1250 (1995).

[5] F. Gittes, B. Schnurr, P. D. Olmsted, F. C. MacKintosh, and C. F. Schmidt, Phys. Rev. Lett. **79**, 3286 (1997).

[6] I. Sriram, E. M. Furst, R. J. DePuit, and T. M. Squires, J. Rheol. **53**, 357 (2009).

[7] I. Sriram, A. Meyer, and E. M. Furst, Phys. Fluids **22**, 062003 (2010).

[8] A. Meyer, A. Marshall, B. G. Bush, and E. M. Furst, J. Rheol. **50**, 77 (2006).

[9] P. Habdas, D. Schaar, A. C. Levitt, and E. R. Weeks, Europhys. Lett. **67**, 477 (2004).

[10] A. R. Bausch, W. Moller, and E. Sackmann, Biophys. J. **76**, 573 (1999).

[11] S. Yamada, D. Wirtz, and S. C. Kuo, Biophys. J. **78**, 1736 (2000).

[12] Q. Lu and M. J. Solomon, Phys. Rev. E **66**, 061504 (2002).

[13] T. G. Mason, K. Ganesan, J. H. vanZanten, D. Wirtz, and S. C. Kuo, Phys. Rev. Lett. **79**, 3282 (1997).

[14] J. H. van Zanten and K. P. Rufener, Phys. Rev. E **62**, 5389 (2000).

[15] B. Schnurr, F. Gittes, F. C. MacKintosh, and C. F. Schmidt, Macromolecules **30**, 7781 (1997).

[16] G. H. Koenderink, M. Atakhorrami, F. C. MacKintosh, and C. F. Schmidt, Phys. Rev. Lett. **96**, 138307 (2006).

[17] F. C. MacKintosh and C. F. Schmidt, Curr. Opin. Colloid Interface Sci. **4**, 300 (1999).

[18] M. Karim, S. C. Kohale, T. Indei, J. D. Schieber, and R. Khare, Phys. Rev. E **86**, 051501 (2012).

[19] D. Weihs, T. G. Mason, and M. A. Teitell, Biophys. J. **91**, 4296 (2006).

[20] M. D. Ediger, Annu. Rev. Phys. Chem. **51**, 99 (2000).

[21] S. K. Lai, Y. y. Wang, D. Wirtz, and J. Hanes, Adv. Drug Delivery Rev. **61**, 86 (2009).

[22] D. R. Paul and L. M. Robeson, Polymer **49**, 3187 (2008).

[23] A. J. Levine and T. C. Lubensky, Phys. Rev. Lett. **85**, 1774 (2000).

[24] A. Córdoba, J. D. Schieber, and T. Indei, Physics of Fluids **24**, 073103 (2012).

[25] A. Córdoba, J. D. Schieber, and T. Indei, Soft Matter **11**, 1 (2015).

[26] U. Yamamoto and K. S. Schweizer, J. Chem. Phys. **135**, 224902 (2011).

[27] T. G. Mason, Rheol. Acta **39**, 371 (2000).

[28] B. R. Dasgupta, S. Y. Tee, J. C. Crocker, B. J. Frisken, and D. A. Weitz, Phys. Rev. E **65**, 051505 (2002).

[29] F. B. Wyart and P. G. de Gennes, Eur. Phys. J. E **1**, 93 (2000).

[30] B. U. Felderhof, J. Chem. Phys. **131**, 164904 (2009).

[31] B. U. Felderhof, J. Chem. Phys. **134**, 204910 (2011).

[32] T. Indei, J. D. Schieber, A. Córdoba, and E. Pilyugina, Physical Review E **85**, 021504 (2012).

[33] T. Indei, J. D. Schieber, and A. Córdoba, Phys. Rev. E **85**, 041504 (2012).

[34] A. Córdoba, T. Indei, and J. D. Schieber, Journal of Rheology **56**, 185 (2012).

[35] K. Xu, M. G. Forest, and I. Klapper, J. Non-Newtonian Fluid Mech **145**, 150 (2007).

[36] R. Zwanzig and M. Bixon, Phys. Rev. A **2**, 2005 (1970).

[37] A. Kuhnhold and W. Paul, Phys. Rev. E **90**, 12, 022602 (2014).

[38] A. Kuhnhold and W. Paul, Phys. Rev. E **91**, 042601 (2015).

[39] J. D. Weeks, D. Chandler, and H. C. Anderson, J. Chem. Phys. **54**, 5237 (1971).

[40] S. C. Kohale and R. Khare, J. Chem. Phys. **129**, 164706 (2008).

[41] S. C. Kohale and R. Khare, J. Chem. Phys. **132**, 234706 (2010).

[42] J. R. Warner, Ind. Eng. Chem. Fundam. **11**, 379 (1972).

[43] D. J. Evans and G. Morriss, *Statistical Mechanics of Nonequilibrium Liquids*, 2nd ed. (Cambridge University Press, UK, 2008).

[44] M. Vladkov and J.-L. Barrat, Macromol. Theory Simul. **15**, 252 (2006).

[45] W. Shinoda, M. Shiga, and M. Mikami, Phys. Rev. B **69**, 134103 (2004).

[46] S. Plimpton, J. Comput. Phys. **117**, 1 (1995).

[47] L. D. Landau and E. M. Lifshitz, *Fluid Mechanics*, 2nd ed., Vol. 6 (Butterworth-Heinemann, London, 1987).

[48] K. Hyun, M. Wilhelm, C. O. Klein, K. S. Cho, J. G. Nam, K. H. Ahn, S. J. Lee, R. H. Ewoldt, and G. H. McKinley, Prog. Polym. Sci. **36**, 1697 (2011).

[49] S. Sen, S. K. Kumar, and P. Keblinski, Macromolecules **38**, 650 (2005).

[50] H. Flyvbjerg and H. G. Petersen, J. Chem. Phys. **91**, 461 (1989).

[51] M. Baumgaertel, A. Schausberger, and H. H. Winter, Rheol. Acta. **29**, 400 (1990).

[52] For $t > \tau_{\max}$, the first term gives a plateau whereas the second term $g_0 f^{(0)}$ is proportional

to t . Therefore, if the height of the plateau is equal to the second term at $t = t_{\max}$, then Eq. (6) is proportional to t for $t > t_{\max}$.

[53] J. Liu, D. Cao, and L. Zhang, J. Phys. Chem. C **112**, 6653 (2008).

[54] A. Tuteja, M. E. Mackay, S. Narayanan, S. Asokan, and M. S. Wong, Nano Lett. **7**, 1276 (2007).

[55] C. A. Grabowski, B. Adhikary, and A. Mukhopadhyay, Appl. Phys. Lett. **94**, 021903 (2009).

[56] C. D. Chapman, K. Lee, D. Henze, D. E. Smith, and R. M. Robertson-Anderson, Macromolecules **47**, 1181 (2014).

[57] J. D. Schieber and M. Andreev, Annual Reviews Chemical and Biomolecular Engineering **5**, 236 (2014).

[58] K. Kremer and G. S. Grest, J. Chem. Phys. **92**, 5057 (1990).

[59] M. Katzarova, L. Yang, M. Andreev, A. Córdoba, and J. D. Schieber, Rheologica Acta **54**, 169 (2015).

[60] M. Andreev, H. Feng, L. Yang, and J. D. Schieber, J. Rheol. **58**, 723 (2014).

[61] M. Rubinstein and R. H. Colby, *Polymer Physics* (Oxford University Press, Oxford, 2010).

[62] R. N. Khaliullin and J. D. Schieber, Macromolecules **42**, 7504 (2009).

[63] R. Jain and T. Stylianopoulos, Nat. Rev. Clin. Oncol. **7**, 653 (2010).

[64] D. Ding, J. Wang, Z. Zhu, R. Li, W. Wu, B. Liu, and X. Jiang, ACS Appl. Mater. Interfaces **4**, 1838 (2012).

[65] J. G. H. Cifre, S. Hess, and M. Kröger, Macromol. Theory Simul. **13**, 748 (2004).

[66] B. H. Zimm, Journal of Chemical Physics **24**, 269 (1956).